Proceedings of the 6th International Conference on Gas Hydrates (ICGH 2008),
Vancouver, British Columbia, CANADA, July 6-10, 2008.

JOINT SEISMIC/ELECTRICAL EFFECTIVE MEDIUM MODELLING OF HYDRATE-BEARING MARINE SEDIMENTS AND AN APPLICATION TO THE VANCOUVER ISLAND MARGIN

M. H. Ellis, T. A. Minshull*, M. C. Sinha and A. I. Best
National Oceanography Centre, Southampton
University of Southampton
Waterfront Campus
European Way, Southampton
SO14 3ZH, UNITED KINGDOM

ABSTRACT

Remote determination of the hydrate content of marine sediments remains a challenging problem. In the absence of boreholes, the most commonly used approach involves the measurement of P-wave velocities from seismic experiments. A range of seismic effective medium methods has been developed to interpret these velocities in terms of hydrate content, but uncertainties about the pore-scale distribution of hydrate can lead to large uncertainties in this interpretation. Where borehole geophysical measurements are available, electrical resistivity is widely used as a proxy for hydrate content, and the measurement of resistivity using controlled source electromagnetic methods shows considerable promise. However, resistivity is commonly related to hydrate content using Archie's law, an empirical relationship with no physical basis that has been shown to fail for hydrate-bearing sediments. We have developed an electrical effective medium method appropriate to hydrate-bearing sediments based on the application of a geometric correction to the Hashin-Shrikman conductive bound, and tested this method by making resistivity measurements on artificial sediments of known porosity. We have adapted our method to deal with anisotropic grains such as clay particles, and combined it with a well-established seismic effective medium method to develop a strategy for estimating the hydrate content of marine sediments based on a combination of seismic and electrical methods. We have applied our approach to borehole geophysical data from Integrated Ocean Drilling Program Expedition 311 on the Vancouver Island margin. Hydrate saturations were determined from resistivity logs by adjusting the geometric factor in areas of the log where hydrate was not present. This value was then used over the entire resistivity log. Hydrate saturations determined using this method match well those determined from direct measurements of the methane content of pressurized cores.

Keywords: gas hydrates, effective medium modelling, velocity, resistivity, Cascadia Margin

NOMENCLATURE

a	tortuosity
G	Geometric factor
L	mean free path length
l_1	deviated path length
l_2	un-deviated path length
m	cementation
r	grain radius
β	volume fraction of the pore fluids
ρ_{geo}	geometrically altered resistivity
ρ_{GPL}	final effective resistivity

ρ_{HS}	Hashin-Shrikman conductive resistivity bound
σ_f	conductivity of the pore fluids
σ_{HS}	Hashin-Shrikman conductive conductivity bound
σ_s	conductivity of the solid grains
φ_c	critical porosity

INTRODUCTION

Gas hydrates are known to affect the physical properties of the sediment in which they form. Hydrate can increase the seismic velocity by replacing the pore fluids and by cementing the grains together. Hydrate also increases the electrical resistivity of the sediments by replacing the conducting pore waters and by blocking pores. The degree of the increase depends on the morphology of the hydrate. This work presents a seismic velocity and electrical resistivity effective medium model to interpret sediments in terms of their porosity, microstructure and gas hydrate saturation. We then apply these models to velocity and resistivity borehole data collected during IODP exp. 311 on Cascadia margin to determine the gas hydrate saturations of the sediments.

SEISMIC MODEL

Two-phase effective medium modelling

After reviewing several different methods of calculating the seismic properties of an Effective Medium we decided to use the combined self-consistent approximation and differential effective medium (SCA/DEM) method developed by Sheng [1,2] and Hornby [3]. The self-consistent approximation (SCA) and the differential effective medium (DEM) methods determine the effective bulk and shear moduli of a medium from the individual components and the geometric relation between those components. Both methods embed inclusions of one material, which may have a variety of shapes, within another material.

The grains and pore fluid in clastic sediments are generally both fully interconnected at all realistic porosities. It is therefore necessary to use a bi-connected effective medium to model such sediments. If a sediment is assumed to be bi-connected at all porosities then individually neither the SCA nor the DEM can model it. The SCA goes through a bi-connected stage at porosities of 40-60% [1,4] but not at other porosities, and should not be used at porosities greater than 60%. The DEM allows the micro-structures to be modelled but it is completely dependent on the starting medium. If the starting medium is solid and fluid inclusions are added, the solid will remain interconnected at all porosities and the fluid will remain isolated. Therefore one or other of the phases is always interconnected and the other is isolated at all porosities preventing the DEM to represent bi-connected sediment.

Sheng [1] used a combination of the SCA and DEM to model a system in which the solid portion of the medium can be load-bearing while the fluid portion remains totally interconnected. This method was developed for sandstones. It starts by calculating the effective bulk and shear moduli for a two phase medium at a critical porosity (φ_c) using the SCA method. The moduli calculated using the SCA method are entered into the DEM technique which then calculates the moduli at all other porosities. Since the DEM preserves the microstructure of its starting medium the final effective medium must also be interconnected at all porosities. Figure 1 shows the change in P-wave velocity with porosity of the SCA/DEM method with 2 different φ_c. It shows the φ_c has a huge effect on the effective P-wave velocity and therefore choosing the correct critical porosity is very important. Sheng [1,2] determined the critical porosity from Archie's [5] equations for resistivity; the critical porosity is related to the tortuosity (a) and cementation (m) by:

$$a = \frac{3\varphi_c - 1}{2\varphi_c^{\ m}} \qquad (1)$$

Sheng [2] uses values of 1 for tortuosity and 2 for cementation. These are generally accepted values for calculating the resistivity of a clean sandstone and give a critical porosity of 0.5. For our purpose the Sheng method has two problems.

(1) We are trying to model sediment in general and not sandstone; a loose sediment has no cementation and therefore m should be equal to 1.25, resulting in a critical porosity of 1 if a =1. This cannot be the case since there can be no bi-connection when there is no solid.

(2) Since Archie's is an empirical relation, the a and the m coefficients do not have direct physical meaning, although they do tell something about the nature of the medium.

Comparing the P-wave velocities calculated using a critical porosity of 0.5 with velocities measured from experimental data (Figure 1), we can see that the combined SCA/DEM method predicts velocities that are

~0.75 kms^{-1} too high at ~0.35 porosity. Therefore we need another method to determine the critical porosity that fits the data better and is not reliant on empirical constants. Greer [6] defines the critical porosity as the point at which the effective medium loses shear strength. Using the SCA method as defined by Willis [7] the effective medium loses its shear strength at ~60% porosity. Setting the critical porosity at this point provides a much better fit to experimental data than using the 50% critical porosity suggested by Sheng (Figure 1). In terms of Archie's equation, tortuosity, calculated using Equation (1) for a critical porosity of 60% and assuming a cementation of 1 (i.e., no cementation) is 0.666, well within the normal range of 0.35-4.78 [8].

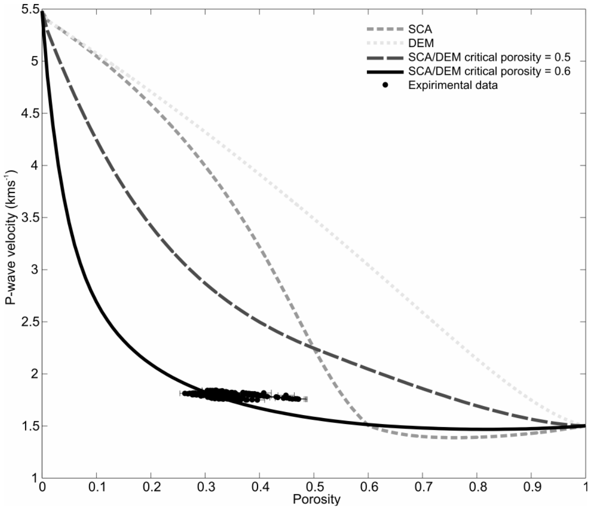

Figure 1. Comparison of the P-wave velocities computed using the SCA, DEM and the combined SCA/DEM with different critical porosities and P-wave laboratory data. P-wave velocity errors for the experimental data are not shown because they are smaller than the markers used in the plot. The velocity errors are estimated to be 0.6% and the porosity errors 3.4%.

Three-phase effective medium modelling

In order to add hydrate into the material we use the method developed by Jakobsen *et al*. [9]. To model non-load bearing hydrate the effective medium model is initially composed of just pore water and grains. The SCA/DEM method is used to calculate the bulk and shear moduli of the 2-phase effective medium. Hydrate is then added in small increments by the DEM method until the prescribed hydrate concentration is achieved. The hydrate only replaces the fluid phase, so amounts of fluid equal to the amount of hydrate added must be removed. The solid grain volume fraction remains the same. The hydrate has the same aspect ratio and orientation as the solid phase. The hydrate simply forms a second set of inclusions within the model with different moduli to those of the first set. However, hydrate inclusions remain isolated from each other at all concentrations.

To determine the effective moduli of a load bearing hydrate phase within the sediments we again use the approach of Jakobsen *et al*. [9]. The method is similar to that for non-load bearing hydrate, except the roles of the hydrate and the pore fluids are reversed. The SCA/DEM method is first used to calculate the effective moduli of a medium containing hydrate and solid, with hydrate taking the place of the pore fluid. The fluid is then added into the effective medium using the DEM method and remains isolated at all porosities. Figure 2 shows the changes in P-wave velocity as hydrate saturation and porosity changes for both the load bearing and non-load bearing methods.

ELECTRICAL MODEL

Hashin-Shtrikman bounds

In order to jointly interpret seismic and electrical data the seismic and electrical models must be compatible. The most common method to interpret resistivity data is to use Archie's [5] equation. However this equation uses empirical constants that have no direct physical meaning. To move away from Archie's equation, we have developed an electrical model based on the Hashin-Strikman (HS) electrical conductive bound [10]. In this model the resistivities of the individual components, the volume fraction of the components, and the geometry of the individual components relative to each other are defined in a similar manner to that of the seismic effective medium model.

The Hashin-Shtrikman (HS) bounds [10] are effective conductivity bounds that give the narrowest possible bounds without defining the geometry between components of a two-phase medium. The conductive bound represents the minimum resistivity the isotropic composite can have. This occurs when the fluid (conductive phase) is totally interconnected and the solid (resistive phase) is totally isolated. The HS conductive bound is given as:

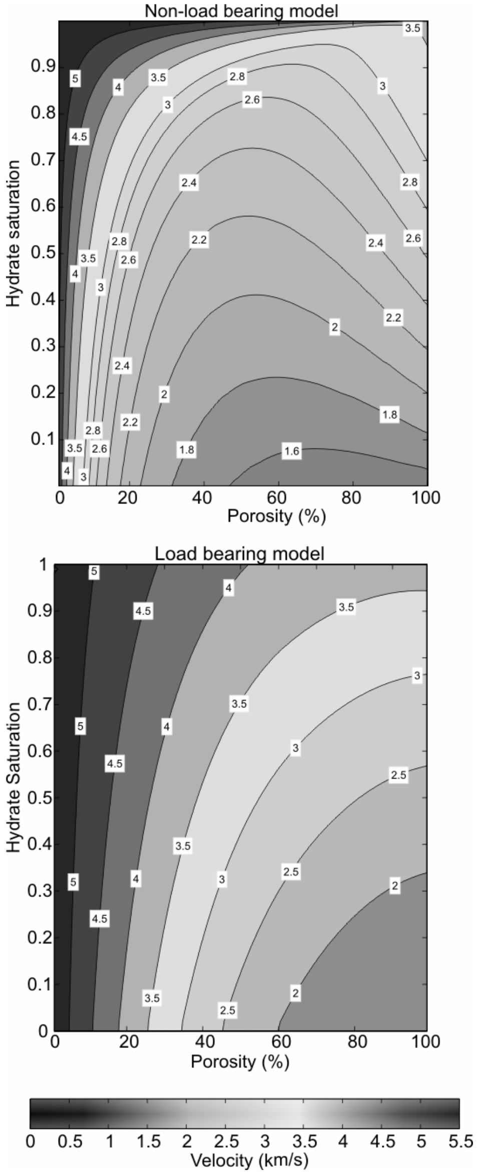

Figure 2 Change in P-wave velocity with hydrate saturation and porosity for the non-load bearing model (top) and the load bearing model (bottom).

$$\frac{1}{\rho_{HS}} = \sigma_{HS} = \sigma_f + (1-\beta)\left(\frac{1}{\sigma_s - \sigma_f} + \frac{\beta}{3\sigma_f}\right)^{-1} \quad (2)$$

where, ρ_{HS} and σ_{HS} are the effective resistivity and conductivity of the composite medium, σ_s and σ_f are the conductivity of the solid grains and the fluid respectively and β represents the volume fraction of the fluid phase.

Geometric factor

The presence of grains in a fluid affects the resistivity in several ways: (1) The grains reduce the cross-sectional area of conduction through which the current must flow. This reduction means that the amount of current that must flow through the resistive phase is increased, and is accounted for in the HS bounds. (2) Since in general the current is no longer directly aligned with the ambient electric field there is an increase in the 'path-length' as the current will preferentially travel around the grains rather than through them. (3) The grain density influences the proportion of the path length that is deviated in order to travel around the grains and the proportion of the path length that is not deviated. This section will investigate the latter two points and will develop an effective medium model that takes into account all three points.

To address point (2) we introduce a geometric factor (*G*) to account for the increase in electrical path length caused by the presence of grains in the fluid. The electric current will take the shortest available route through the sediment but this is longer than the actual length of sediment because the current must go around the grains. It is assumed that when the current encounters the grain it will travel around the grain until it reaches a point at which it can continue in the fluid along the same path (Figure 3). The geometric path length is the ratio of the deviated path length (l_1) to the un-deviated path length (l_2) around the grain. The current will not encounter grains at the same point on each grain and therefore must be calculated at every point over the grain cross-section to produce an average geometric factor. The geometric factor is then applied to the σ_f, effectively reducing the σ_f and increasing the final effective resistivity.

$$\frac{1}{\rho_{geo}} = \frac{\sigma_f}{G} + (1-\beta)\left(\frac{1}{\sigma_s - \frac{\sigma_f}{G}} + \frac{G\beta}{3\sigma_f}\right)^{-1} \quad (3)$$

where, ρ_{geo} is the effective resistivity of the medium where the geometric factor is applied in full.

Mean free path length

The geometric factor cannot simply be applied to the HS conductive bound at all porosities because as this would cause the estimated resistivity of the medium to be greater than the resistivity of the fluid at 100% porosity. Therefore a method is needed to determine the percentage of the fluid to which the geometric factor must be applied, so that at 100% porosity the geometric factor is equal to unity.

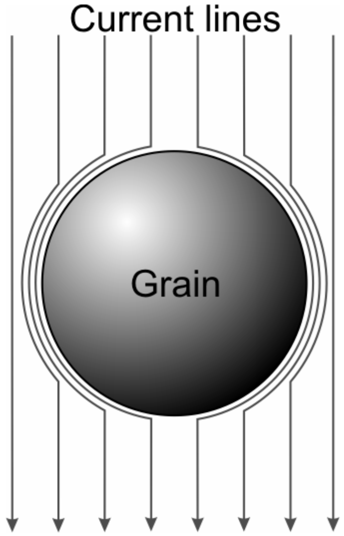

Figure 3 Deviation of current as it passes a spherical grain.

The current will spend a certain proportion of the total path length deviated around the grains, with the remainder of the path length un-deviated. The individual proportions will depend on the porosity of the sediment. Calculating the proportions of the total length that the current spends deviated and un-deviated allows us to navigate between the geometrically altered bound and the conductive HS bound. To calculate the average distance between the grains (L), an adapted version of the mean free path, which is used in the kinetic theory of gases to calculate the average distance between molecule collisions, can be used.

$$L = \frac{4r}{3(1-\beta)} \qquad (4)$$

This can then be used with l_2 to determine what percentage of the total length the current spends going around the grains. Because L and l_2 are both proportional to the radius of the grains, the un-deviated and deviated proportions are independent of the grain size. These proportions can now be used to navigate between ρ_{HS} and ρ_{geo} to give a final effective resistivity.

$$\frac{1}{\rho_{GPL}} = \left(\frac{1}{\rho_{HS}}\frac{l_2}{L}\right) + \left(\frac{1}{\rho_{geo}}\left(1-\frac{l_2}{L}\right)\right) \qquad (5)$$

Adding hydrate

As with the seismic modelling, hydrate can be added into the model in two ways. In the first case gas hydrate is modelled as isolated grains within the fluid. The resulting change in resistivity is due to the replacement of the conducting pore fluids only and not the blocking of pore throats. In the second case the hydrate replaces the pore fluids and blocks pore throats so that the conducting fluid exists as isolated droplets within the medium. This blocking causes higher resistivities than in the first case.

To model the case where hydrate lies within the pore spaces, the hydrate is modelled as a second set of grains within the effective medium. As with the sediment grains the gas hydrate has a much higher resistivity than the fluid. The current will pass primarily through the fluid and not the hydrate. Therefore we adjust the volume fraction of the fluid to exclude that of the hydrate. We now effectively have only one grain type in the effective medium. The resistivity of this grain type is based on the relative proportions of the hydrate and grain solid resistivities. This is a relatively simplistic approach to obtain a grain/hydrate mixture resistivity, but can be used because the final effective medium resistivity is quite insensitive to the resistivity of the solid.

An alternative effective medium model for the distribution of hydrate is one in which the hydrate blocks the connections between adjacent pore spaces. Modelling this case can again be achieved in two steps. First a two-phase effective medium is calculated in which only hydrate and grains exist, similar to the starting model of the load-bearing seismic model. Although the resistivity of the hydrate is high compared to the pore fluids, it is many orders of magnitude lower than the grain. Therefore the electrical current will preferentially travel through the hydrate in the same manner as it travels through the fluid in the fluid/grain case. Then fluid is then added to the required porosity using the HS resistivity bound.

APPLICATION TO CASCADIA MARGIN SEDIMENTS

Integrated Ocean Drilling Program (IODP) Expedition 311 took place in September–October

2005. The area under investigation was the accretionary prism of the Cascadia Subduction zone off the coast of Vancouver Island (Figure 4). The accretionary prism is the result of the Juan de Fuca plate subducting under the North American plate. This location is well known for the widespread abundance of gas hydrates in the continental margin sediments and has been the subject of numerous geophysical studies [11, 12, 13, 14, 15] The principle objective of the expedition was to constrain geological models for the formation of gas hydrates in subduction zone accretionary prisms. This objective required high-quality data on the vertical and regional concentrations and distributions of gas hydrates within the accretionary prism. To this end four sites (U1325, U1326, U1327 and U1329) were drilled and cored along a transect perpendicular to the margin (Figure 4). These sites represented four different stages in the evolution of the gas hydrate stability zone. A fifth site (U1328) was drilled at an active cold vent near site U1327.

At each site logging while drilling (LWD), coring and wireline logging took place, apart from site U1329 where wireline logging was not accomplished. In general 4-5 boreholes were drilled at each site labelled A-E. The first borehole drilled at each site (Borehole A) was solely dedicated to LWD measurements. These measurements included resistivity, porosity, natural gamma ray and density. Boreholes B-E were used for sediment coring and then wireline logging. The cored sediments were subject to a suite of shipboard measurements. These included core temperature measurements using IR images immediately after core retrieval, physical properties measurements, sediment lithology descriptions, interstitial water (IW) geochemistry analyses and void gas geochemistry. The physical property measurements included non-contact and contact resistivity, velocity, shear strength, and moisture and density (MAD) analysis where wet and dry density and porosity can be measured. Wireline logging measurements, which often took place in the same borehole as the coring, included resistivity, porosity and P- and S-wave velocity.

Hydrate saturation from resistivity logs

To determine the hydrate saturation of the sediments the pore fluid and porosity must known. Porosity, which was measured by several techniques, was determined from the Density LWD log. This log was chosen rather than the neutron log because it matched the discreet MAD samples taken from the core. Fluid resistivity was determined from chorinity and downhole temperature measurements, and the equations of Fofonoff [16].

Hydrate saturations were calculated using the geometric path-length non-pore-blocking effective resistivity model ($\rho_{GPLnon\text{-}block}$) as opposed to the pore blocking model ($\rho_{GPLblock}$). Resistivities calculated using the pore blocking method were far too high when compared to the formation resistivities measured in the logs.

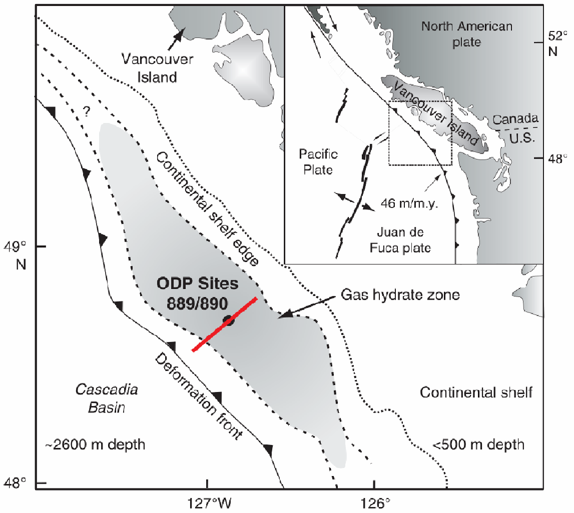

Figure 4 General location of IODP Expedition 311 drilling transect (red line) near the previous ODP Sites 889/890 off the coast of Vancouver Island. A bottom-simulating reflector is present on ~50% of the mid-continental slope (shaded area) [17].

To use the geometric path-length non-pore-blocking effective resistivity method an aspect ratio must be used within the equations. However, in continental margin sediments the average aspect ratio is very difficult to determine and the alignment of the grains is also problematic. To determine a sensible aspect ratio and geometric factor we first look at the resistivity log and determine depths where hydrate is not believed to be present. Hydrate is unlikely to be present below the BSR or where resistivity has not increased above background levels. Figure 5.A shows potential depth intervals without hydrate on the resistivity log for site U1327. An aspect ratio is then determined so that the resistivity gives a hydrate saturation of zero for these areas. This aspect ratio and corresponding geometric factor can then be applied to the whole log. Figure 5.D-F shows predicted hydrate saturations using different possible aspect ratios and geometric factors. Figure 5.D shows an aspect ratio that is too high and gives high hydrate saturations throughout the sediment column even at depths where hydrate cannot be present. Figure 5.F shows the hydrate saturations when too low an aspect ratio is used leading to an underestimation the hydrate content. Figure 5.E shows the results when the aspect ratio is adjusted so that zero hydrate saturation is predicted for the background resistivity, leaving an interval of increased hydrate saturation which corresponds to the resistivity increase on the resistivity log.

Hydrate saturation from velocity logs

To use the SCA/DEM method to solve for hydrate saturation the porosity, individual moduli of the components and the grain aspect ratio must be known. The porosity and aspect ratio values used are the same as those used for the resistivity calculations. The bulk and shear moduli of hydrate and brine are well constrained. The composition of the grains in the matrix is important when determining the hydrate saturation from the seismic velocities. Hobro *et al.* [13] use a sediment grain composition of 35% clay, 20% quartz and 45% feldspar to determine hydrate saturations. Chen [18] and Riedel *et al.*, [19] use a much higher clay fraction of 85% with the rest of the sediment being composed of quartz. Based on smear slide data obtained from the cores, we use a sediment composition that is predominantly clay (~80%) with smaller amounts of quartz, feldspar and biogenic opal. The bulk and shear moduli of clay are very hard to measure due to the small size of the grains. Clay bulk modulus values between 20 GPa and 50 GPa have been reported [20]. A bulk modulus of 20.9 GPa and a shear modulus of 6.9 GPa commonly have been used to interpret seismic velocity data [21, 22] and are used here.

Hydrate saturations

Figure 6 shows the LWD and wireline derived hydrate saturations for both velocity and resistivity across the margin transect (sites U1326, U1325, U1327 and U1329). Wireline measurements are made after the borehole has been drilled, unlike the LWD measurements. Therefore the time delay and/or the disturbance to the sediments may cause some discrepancy between the two logging measurements.

At site U1326 both the wireline and the LWD resistivity logs record the maximum hydrate saturation at 90 m below the sea floor, well above the predicted BSR. At this point the predicted hydrate saturation is approximately 90%. This observation is contrary to the predictions of numerical models such as that of Hyndman and Davis [23] and of Buffett & Archer [24] of maximum hydrate saturation just above the BSR. Throughout the rest of the sediment column the mean hydrate saturation is 9%. Maximum hydrate saturation occurs much deeper in the sediment column at site U1325. It occurs between 190 m and 230 m depth and is just above the BSR. Maximum hydrate saturation occurs at site U1327 in a very distinctive band between 120 and 140 m depth (Figure 6). Hydrate saturations calculated from the LWD resistivities indicate that the saturations are approximately 70% in this area. The very high hydrate saturation is not seen to the same extent in the wireline logging calculations where hydrate saturations of approximately 20% are inferred. Table 1 gives a summery of the gas hydrate saturations for each to the sites.

	ρ LWD	**ρ Wireline**	***Vp***	***Vs***
Site U1325	0.02	0.04	0.02	0.02
Site U1326	0.09	0.07	0.19	0.06
Site U1327	0.06	0.11	0.07	0.11
Site U1328	0.06	0.06	0.03	0.07
Site U1329	0.06	-	-	-

Table 1. Mean gas hydrate saturations throughout the logged sedimentary columns at each of the sites calculated using the SCA/DEM model and the Geometric Path-Length Effective Resistivity model.

Hydrate saturations appear to steadily increase with depth at site U1329A. A saturation of 40% is inferred at a depth of 200 m, well below the predicted BSR depth of 129 m. At all of the sites hydrate is inferred to be present below the BSR. The BSR depth is well constrained in this area and is unlikely to be incorrect by more than 10 m, so another explanation must be sought. A possibility is that free gas is present in the sediments below the BSR. Free gas also causes the resistivity of the sediments to increase. The geometric path-length model assumes that the changes in resistivity are due solely to the presence of hydrate, but free gas would have a similar effect. Sonic log studies of data obtained during ODP Exp. 146 indicate that some free gas must be present beneath the BSR in the region of site U1327 and U1328. MacKay *et al.* [25] estimate free gas concentrations of 1-5% to account for the low velocities observed below the BSR. Figure 6 also shows velocity derived gas hydrate calculations for each of the sites across the transect. There are unfortunately no velocity data available for site U1329.

Hydrate saturations appear to be very laterally discontinuous across the transect. Even within the same site, different boreholes show very different hydrate saturations. Site U1327 is a prime example. The LWD resistivities indicate a thick zone of high hydrate saturation which does not appear on the velocity or the resistivity wireline logs. The LWD logging always was measured in a separate borehole to the wireline logs. These boreholes were generally about 20 m apart, indicating a high degree of heterogeneity in the sediments. The prediction that the maximum hydrate saturations should occur just above the BSR does not seem to be the common case along this transect. Maximum hydrate concentrations occur higher in the sediment column at most of the sites.

Downhole logging data from a previous expedition (ODP exp. 146, sites 889/890) in the same area has been used to determine the gas hydrate saturations. Saturations may reach up to 30% of the pore space in a region 100 m above the BSR [26, 27 28]. Other estimates have put the hydrate concentrations at 20-35% [29, 30]. If such concentrations exist then they are far higher than other margins studied [31]. Blake Ridge saturations are thought to be less than 10% [32] and Hydrate Ridge they are thought to be less than 5% [33]. Ussler & Paull [34] estimated much lower hydrate saturations from the chorinity data from Exp. 146. Gas hydrate saturations have recently been recalculated from the Exp. 146 logging data and the chorinity data by Riedel *et al.* [31] indicating hydrate values of 5-10%. Using a three-dimensional topographic seismic study Hobro *et al.* [13] estimate an even lower mean hydrate saturation of 2% with a maximum hydrate saturation of 15%. Yuan & Edwards [35] used EM methods to determine hydrate saturations near ODP site 889A (near IODP sites U1327 and U1328). They estimate that the hydrate saturation is 17-36% 100m above the BSR. Chen [18] also derives hydrate saturation using the data collected during Exp. 311. Chen's [18] values of mean hydrate saturation are similar to the values obtained during this work although different models were used. Data from Exp. 311 using the above methods indicate that the hydrate saturations vary from a few percent to a maximum of 60% of the pore space in some very localized areas. Seismic methods put the average hydrate saturation at 2-19% across all the sites. Electrical methods estimates for the average hydrate saturations range from 2-11% across all of the sites. Results from the analysis in this work indicate that hydrate saturations on the Cascadia margin are towards the lower end of the range of reported hydrate saturations.

For completeness data from site U1328 were also analyzed. Site U1328 was drilled at a cold vent off the transect line. It has been identified as a cold vent by vertical seismic blanking and is associated with near-surface faults [19,36]. The area has also been extensively cored [37,38]. These cores sampled massive gas charged hydrates. However due to the stiff hydrate preventing further penetration of the sediments the thickness of the massive hydrate cap could not be established [38]. This area has also been the subject of EM studies that indicate high resistivities at the vent site [35,39]. As a result gas hydrate was expected to be concentrated in the top few metres as a cap over the sediments. Hydrate saturation calculated here from the resistivity LWD log is approximately 40% at the surface and decreases with depth until it disappears completely by 50m below the sea floor (Figure 6). Comparing the wireline resistivity derived hydrates saturations to those from the LWD shows a similar overall pattern. The wire line log misses the top 55 m of the sediment column which is why the high hydrate saturations are not observed on the wireline log. The velocity data indicates that there is very little hydrate along the entire length of the log. However the velocity log also misses the top 55m of the sediment column.

CONCLUSION

Non-load bearing gas hydrate is present at each of the sites. Apart from site U1325 the hydrate does not appear to be concentrated just above the BSR as suggested by Hyndman & Davis (1992). Gas hydrate saturation was low (2-9%) at all sites apart from Site U1326 where a mean gas hydrate saturation of 14% was calculated. Hydrate calculations for the cold vent site were similar to those determined by Riedel *et al.,* (2005) although peak hydrate saturation in the very top sediments were calculated to be approximately 80%. Mean gas hydrate saturations calculated using the methods described above indicates that hydrate saturations are towards the lower end of estimates put forward in the literature for this margin.

REFERENCES

[1] Sheng, P., 1990, *Effective-medium theory of sedimentary rocks,* Physical Review B**, 41**, 4507-4512.

[2] Sheng, P., 1991, *Consistent modelling of the electrical and elastic properties of sedimentary rocks,* Geophysics, **56(8),** 1236-1243.

[3] Hornby, B.E., Schwartz, L.M. & Hudson, J.A., 1994. *Anisotropic effective-medium modelling of the elastic properties of shales,* Geophysics, **59**, 1570-1581.

[4] Berryman, J., 1980, Long-wavelength propagation in composite elastic media I. Spherical inclusions. *Journal of the Acoustical Society of America*. **68**, 1809-1819.

[5] Archie, G.E., 1942, *The electrical resistivity log as an aid in determining some reservoir characteristics,* Transactions of the American Institute of Mining Engineers, **146**, 54-62.

[6] Greer, A.A., 2001, *Joint Interpretation of seismic and electromagnetic results, investigating zero age oceanic crust.*, PhD thesis. University of Cambridge.

[7] Willis, J.R., 1977, *Bounds and self-consistent estimates for the overall properties of anisotropic composites.* Journal of the Mechanics and Physics of Solids., **25**, 185-202.

[8] Bassiouni, Z., 1994, *Theory, Measurement, and Interpretation of Well Logs,* Society of Petroleum Engineers, Richardson, Texas,

[9] Jakobsen, M., Hudson, J.A., Minshull, T.A. & Singh, S.C., 2000, *Elastic properties of hydrate-bearing sediments using effective medium theory,* Journal of Geophysical Research., **105**, 561-577.

[10] Hashin, Z. & Shtrikman, S., 1962, *A variational approach to the theory of the effective magnetic permeability of multiphase materials,* Journal of Applied. Physics, **33**, 3125–3131.

[11] Chapman, N.R., Gettrust, J.F., Walia, R., Hannay, D., Spence, G.D., Wood, W.T., & Hyndman, R.D., 2002., *High-resolution, deep-towed, multichannel seismic survey of deep-sea gas hydrates off western Canada,* Geophysics, **67**, 1038-1047.

[12] Hyndman, R.D. & Spence, G.D., 1992, *A seismic study of methane hydrate bottom simulating reflectors,* Journal of Geophysical Research, **97**, 6683-6698.

[13] Hobro, J.W.D., Minshull, T.A., Singh, S.C. & Chand, S., 2005, *A three-dimensional seismic tomography study of the gas hydrate stability zone, offshore Vancouver Island,* Journal of Geophysical Research, **110**, B09102,

[14] Riedel, M., Hyndman, R.D., Spence, G.D. & Chapman, N.R., 2002, *Seismic investigations of a vent field associated with gas hydrates, offshore Vancouver Island,* Journal of Geophysical Research, **107**, 2200.

[15] Westbrook, G.K., Carson, B., Musgrave, R. & Shipboard Scientific Party, 1994, Proceedings of the Ocean Drilling Program, Initial Reports, **146**.

[16] Fofonoff, N.P., 1985, *Physical properties of seawater: a new salinity scale and of state for seawater,* Journal of Geophysical Research, **90**, 3332-3342.

[17] Riedel, M., Collett, T., Malone, M., & Shipboard Scientific Party 2006. Proceedings of the Integrated Ocean Drilling Program, expedition reports, Casdadia margin gas hydrates. ODP, College Station, Texas. 311.

[18] Chen, M-A. P., 2006, *Northern Cascadia Marine Gas Hydrate: Constraints from Resistivity, Velocity, and AVO, MSc Thesis,* University of Victoria.

[19] Riedel, M., Spence, G.D., Chapman, R.N. & Hyndman, R.D., 2001. *Deep sea gas hydrates on the Northern Cascadia margin,* Leading Edge **20**, 87–91.

[20] Vanorio, T., Prasad, M. & Nur, A., 2003, *Elastic properties of dry clay mineral aggregates, suspensions and sandstones,* Geophysical Journal International, **155,** 319–326.

[21] Chand, S., Minshull, T.A., Priest, J.A., Best, A.I., Clayton, C.R.I. & Waite, W.F., 2006, *An effective medium inversion algorithm for gas hydrate quantification and its application to laboratory and borehole measurements of gas hydrate-bearing sediments,* Geophysical Journal International, **166,** 543–552.

[22] Carcione, J.M. & Gei, D., 2004, *Gas hydrate concentration estimated from P- and S-wave*

velocities at the Mallik 2L-38 research well, Mackenzie Delta, Canada, Journal of Applied Geophysics, **56**, 73–78.

[23] Hyndman, R.D. & Davies E.E., 1992, *A Mechanism for the formation of methane hydrate and sea-floor Bottom simulating reflectors by vertical fluid expulsion.* Journal of Geophysical Research-Solid Earth 97, 7025-7041.

[24] Buffett, B., & Archer D., 2004, *Global inventory of methane clathrate: sensitivity to changes in the deep ocean,* Earth and Planetary Science Letters, **227** 185–199.

[25] MacKay, M.E., Jarrard, R.D., Westbrook, G.K. & Hyndman, R.D., 1994, *Origin of bottom-simulating reflectors: geophysical evidence from the Cascadia accretionary prism,* Geology, **22(5),** 459–462.

[26] Hyndman, R.D., Spence, G.D., Chapman, N.R., Riedel, M., & Edwards, R.N., 2001, *Geophysical Studies of Marine Gas Hydrate in Northern Cascadia, In C.K. Paull & W.P. Dillon, (eds.), Natural gas hydrates: occurrence, distribution, detection,* American Geophysical Union Monographs, **124**, 273-295.

[27] Hyndman, R.D., Yuan, T. & Moran, K., 1999, *The concentration of deep sea gas hydrates from downhole electrical resistivity logs and laboratory data,* Earth and Planetary Science Letters, **172,** 167-177.

[28] Spence, G.D. Hyndman, R.D., Chapman, N.R., Riedel, M., Edwards, N., & Yuan, J., 2000, *Cascadia margin, northeast Pacific Ocean: hydrate distribution from geophysical investigations. In Max, M.D. (ed.), Natural Gas Hydrate in Ocean and Permafrost Environments:* Kluwer Academic Publisher, 183–198.

[29] Yuan, T., Hyndman R.D., Spence G.D. & Desmons, B., 1996, *Velocity structure of a bottom-simulating reflector and deep sea gas hydrate concentrations on the Cascadia continental slope,* Journal of Geophysical Research, **101**, 13655-13671.

[30] Yuan, T., Spence, G.D., Hyndman, R.D., Minshull T.A. & Singh, S.C., 1999, *Seismic velocity studies of a gas hydrate bottom-simulating reflector on the northern Cascadia continental margin, Amplitude modeling and full waveform inversion:* Journal of Geophysical Research, **104**, 1179-1191.

[31] Riedel, M., Collett, T., Malone, M., & the Expedition 311 Project Team, 2005, *Cascadia margin gas hydrates,* IODP Scientific Prospectus, **311**.

[32] Paull, C.K. Matsumoto, R. Wallace, P.J. *et al.*, 1996, Proceeding of the ODP, in: Initial Reports, College Station, TX., **164**.

[33] Tréhu, A.M., Bohrmann, G., Rack, & Shipboard Scientific Party, 2004. *Three-dimensional distribution of gas hydrate beneath southern Hydrate Ridge: constraints from ODP Leg 204.* Earth Planetary. Science. Letters. 222, 845– 862.

[34] Ussler, W., & Paull, C.K., 2001, *Ion exclusion associated with marine gas hydrate deposits.* In Paull, C.K., & Dillon, W.P. (eds.), *Natural Gas Hydrates: Occurrence, Distribution, and Detection.* Geophysics. Monograph, **124,** 41–51.

[35] Yuan, J., & Edwards R.N., 2000, *The assessment of marine gas hydrates through electronic remote sounding: Hydrate without a BSR?,* Geophysical. Research Letters., **27**, 2397–2400.

[36] Wood, W.T., Holbrook, W.S. & Hoskins, H., 2000, *In situ measurements of P-wave attenuation in the methane hydrate- and gas-bearing sediments of the Blake Ridge*, Proceedings of the ODP, Scientific Results, **164**, 365-272.

[37] Novosel, I., 2002, *Physical and sedimentological properties of gas hydrate related sediments, offshore Vancouver Island. MSc Thesis,* University of Victoria.

[38] Novosel, I., Spence, G.D. & Hyndman T.R.D., 2005, *Reduced magnetization produced by increased methane flux at a gas hydrate vent,* Marine Geology, **216,** 265– 274.

[39] Schwalenberg, K., Willoughby, E.C., Mir, R., & Edwards, R.N., 2005. *Marine gas hydrate electromagnetic signatures in Cascadia and their correlation with seismic blank zones,* First Break, **23**, 57-63.

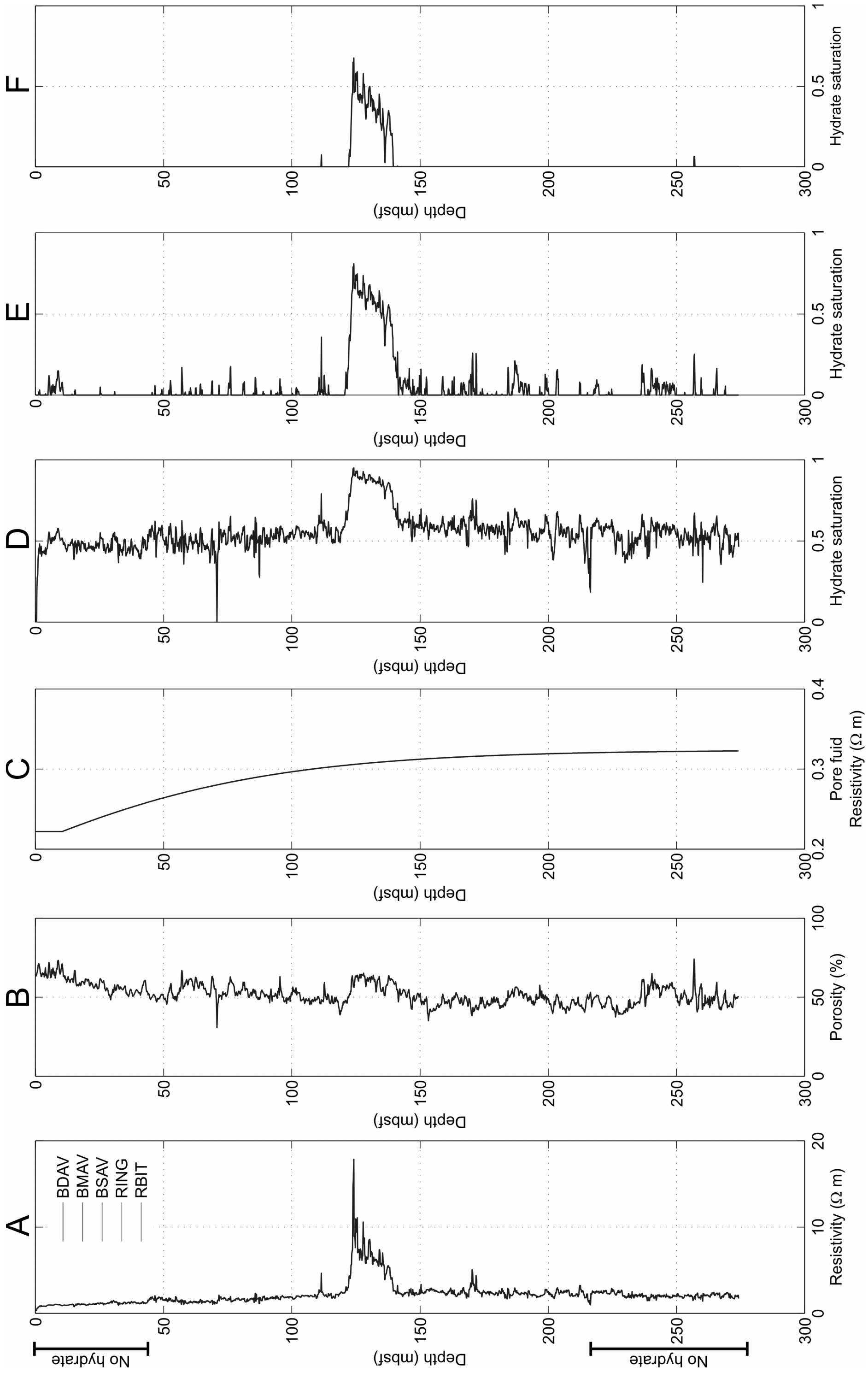

Figure 5. Logging and gas hydrate saturations (calculated from the geometric path-length effective resistivity method) for site U1327. (A) LWD resistivity logs; (B) Density porosity log; (C) Resistivity of the pore fluid; (D) Gas hydrate saturation calculated using a geometric factor of 1.17 and aspect ratio of 1; (E) Gas hydrate saturation calculated using a geometric factor of 6.9 and aspect ratio of 0.1; (F) Gas hydrate saturation calculated using a geometric factor of 13.6 and an aspect ratio of 0.05**.**

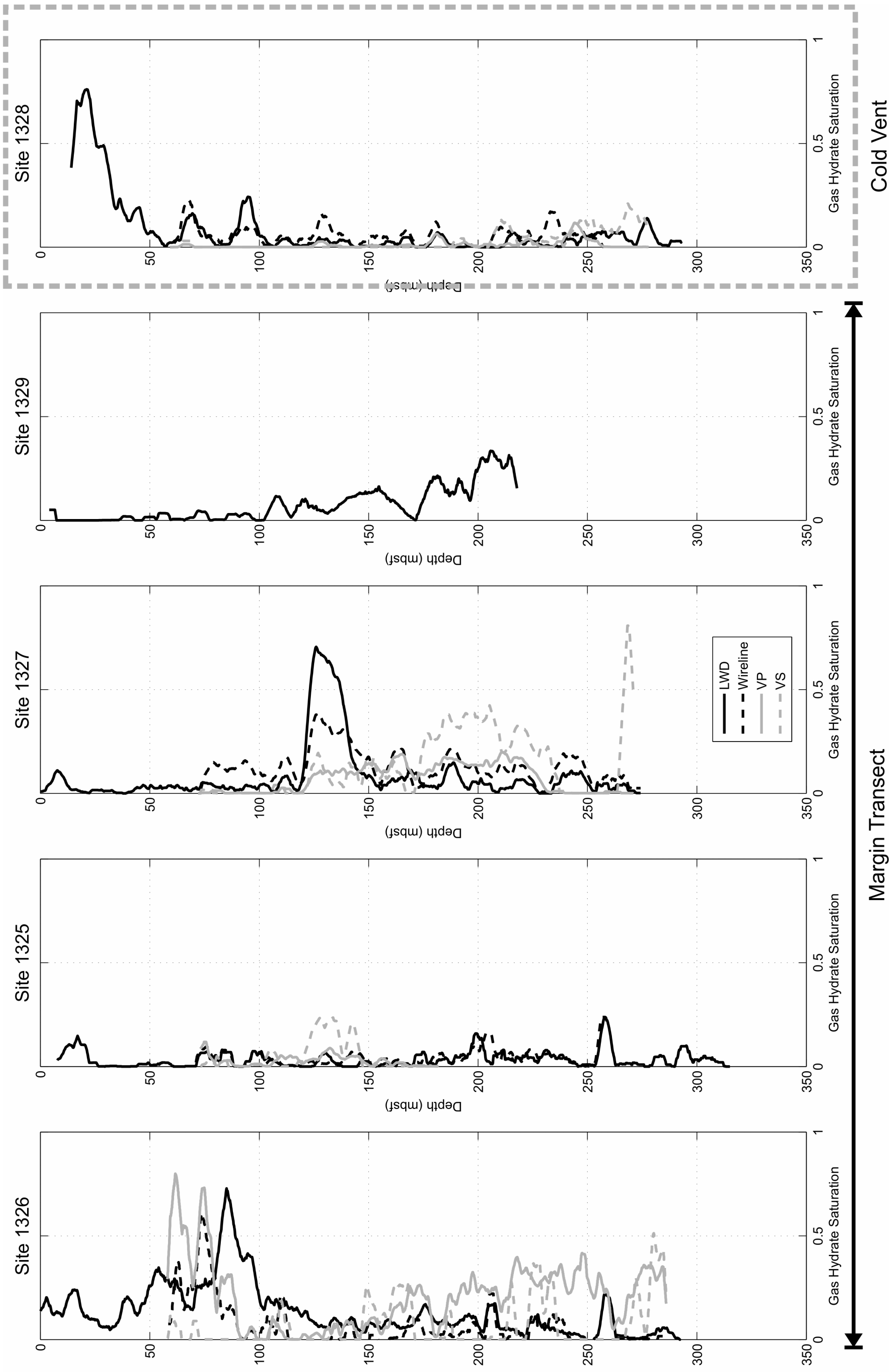

Figure 6. Gas hydrate saturations determined using the LWD resistivity logs and the wireline velocity and resistivity logs.